PHILOSOPHICAL TRANSACTIONS A

royalsocietypublishing.org/journal/rsta

Research

Cite this article: Abbasi A, Sano TG, Yan D, Reis PM. 2023 Snap buckling of bistable beams under combined mechanical and magnetic loading. *Phil. Trans. R. Soc. A* **381**: 20220029. https://doi.org/10.1098/rsta.2022.0029

Received: 18 July 2022
Accepted: 26 October 2022

One contribution of 13 to a theme issue 'Probing and dynamics of shock sensitive shells'.

Subject Areas:
mechanics, mechanical engineering, materials science

Keywords:
magneto-rheological elastomers, hard-magnetic beams, bistability, snap-through actuation

Author for correspondence:
Pedro M. Reis
e-mail: pedro.reis@epfl.ch

Electronic supplementary material is available online at https://doi.org/10.6084/m9.figshare.c.6373197.

THE ROYAL SOCIETY PUBLISHING

Snap buckling of bistable beams under combined mechanical and magnetic loading

Arefeh Abbasi[1], Tomohiko G. Sano[1,2], Dong Yan[1] and Pedro M. Reis[1]

[1]Flexible Structures Laboratory, Ecole Polytechnique Fédérale de Lausanne (EPFL), Lausanne 1015, Switzerland
[2]Department of Mechanical Engineering, Keio University, Yokohama, Kanagawa, 2230061, Japan

DY, 0000-0002-7988-3031; PMR, 0000-0003-3984-828X

We investigate the mechanics of bistable, hard-magnetic, elastic beams, combining experiments, finite-element modelling (FEM) and a reduced-order theory. The beam is made of a hard magneto-rheological elastomer, comprising two segments with antiparallel magnetization along the centreline, and is set into a bistable curved configuration by imposing an end-to-end shortening. Reversible snapping is possible between these two stable states. First, we experimentally characterize the critical field strength for the onset of snapping, at different levels of end-to-end shortening. Second, we perform three-dimensional FEM simulations using the Riks method to analyse high-order deformation modes during snapping. Third, we develop a reduced-order centreline-based beam theory to rationalize the observed magneto-elastic response. The theory and simulations are validated against experiments, with an excellent quantitative agreement. Finally, we consider the case of combined magnetic loading and poking force, examining how the applied field affects the bistability and quantifying the maximum load-bearing capacity. Our work provides a set of predictive tools for the rational design of one-dimensional, bistable, magneto-elastic structural elements.

This article is part of the theme issue 'Probing and dynamics of shock sensitive shells'.

1. Introduction

The buckling of slender structures has long been a research subject in the structural mechanics community [1]. For example, the buckling of thin shells, which become unstable due to a subcritical bifurcation [2,3], can result in the catastrophic loss of their load-bearing capacity and abrupt changes of the deformation mode. To characterize the stability conditions of shells non-destructively, a diagnostic method using secondary poking forces has recently received much attention [4–7]. In this method, a poking force probes the stability landscape of the structure while its level of compression is varied systematically [2]. Bistable beams can also buckle catastrophically as they snap from one stable state to another [8]; this is the topic of the present work, where we seek to investigate how the snap-through buckling of a bistable hard-magnetic beam, at different levels of an external magnetic loading, couples with an additional mechanical poking force.

Bistable structures are central in the design of many functional devices [9–13], whose internal energy comprises two minima, separated by a maximum, representing the barrier to a fast transition between two stable states. This snap-through instability can be exploited to cause relatively large displacements, or rotations, with low work for actuation, offering potential applications in several engineering domains, including micro-electromechanical systems [14,15], robotics [16,17], energy harvesting [18,19], actuators [20,21], origami structures [22,23] and deployment mechanisms [24]. Bistable beams can be classified into two categories [25]: (i) pre-shaped, which do not possess residual stresses and (ii) pre-compressed, which are stressed post-production to exhibit the first buckling-mode configuration [26]. The latter have gained much attention due to their manufacturability and versatility [21,27,28]. Next, we provide an overview of recent research centred on pre-compressed beams, the type central to our study.

Many past studies on pre-compressed beams have focused on their snap-through characteristics [14,15,26,29,30]: the critical load and displacement, and the travel distance from the first stable state to the new configuration. These features can be set by design parameters; e.g. the beam geometry, end-to-end shortening [14], actuation loading and position [31–38] and boundary conditions [28,33,34,39]. A recently emerging trend in the field of bistable beams is the usage of active materials with external stimuli to control the stability during snap-through by inducing local strains from temperature gradients, swelling or electric/magnetic fields. For example, electrostatic [40,41], piezoelectric [42] and magnetic [43,44] actuation have all been used to control the bistability.

More specifically, there has been a burgeoning interest in magneto-rheological elastomers (MREs), comprising magnetically permeable micron-sized particles embedded into a polymeric matrix, with a mechanical response that can be tuned under an external magnetic field [45,46]. Structures made out of MREs offer opportunities for fast, reversible and remotely controlled shape-shifting behaviour [47–56]. Based on the magnetic response of the embedded particles to applied magnetic fields, MREs are classified into two groups, soft-MREs (s-MREs) or hard-MREs (h-MREs), each of which is discussed next. In s-MREs, an external magnetic field [57] modifies the particles' magnetization, which vanishes when the external field is removed. By contrast, in h-MREs, the focus of the present study, the particles possess a high coercivity to resist demagnetization by external fields upon field saturation [53,57] and their remnant magnetization can be retained during actuation. In particular, flexible slender structures made of h-MREs are capable of significant shape changes, driven by the magnetic body torques induced by the interaction between the intrinsic magnetization of the material and the applied field [51,58]. The magnetization profile of h-MRE structures can be designed by the local orientation of the magnetized particles to generate complex three-dimensional-shape transformations and optimize the shape-shifting modes for specific applications [51,55,58–62].

Owing to the elasticity-magnetism coupling, together with the underlying geometric nonlinearities, modelling the mechanical behaviour of hard-magnetic soft structures is challenging but there have recent advances in this direction. A continuum theory has been developed [63] for the finite deformation of three-dimensional (bulk) h-MREs through a nonlinear magneto-mechanical constitutive law. In this framework, the Helmholtz free energy density includes elastic (neo-Hookean) and magneto-elastic terms. A simulation framework by the same authors using finite-element modelling (FEM) was also developed. Subsequently. a full-field three-dimensional continuum model for h-MREs was proposed [64], also incorporating magnetic dissipation, particle–particle interactions and the surrounding air effects. They validated their model by performing microscopic homogenization simulations applied to macroscopic boundary value problems. Based on the three-dimensional continuum model, and using dimensional reduction, theories for inextensible, hard-magnetic elastica were derived and validated against experiments, under either a uniform magnetic field [55,58] or a field with constant gradient [65]. A similar dimensional reduction approach was applied to model the three-dimensional deformation of hard-magnetic rods under uniform and gradient magnetic fields [66,67]. Considering the extensibility of the centreline, a geometrically exact beam model under uniform fields was developed to predict the deformation of cantilever beams [60,61,68], albeit finding negligible differences with the inextensible model. A similar strategy based on dimensional reduction was employed to capture the behaviour of magnetic thin plates [69], and predict the axisymmetric deformation of pressurized hard-magnetic shells [70]. This one-dimensional shell model was later generalized in a three-dimensional configuration [71].

Even if there have been several studies on modelling the deformation of magneto-active structures, their instability and, more specifically, the snap-through phenomenon under magnetic actuation remains an ongoing research topic. Important questions to address include predicting how bistable systems switch between stable configurations under a magnetic field and evaluating the contributions of the various buckling modes and energy levels to this transition, the elastic counterparts of which have been studied extensively [14,29,72,73]. Additionally, theoretical and computational tools are needed to predict the critical conditions and snap-through response of magneto-active structures. Such developments would be valuable for the predictive and rational design of bistable magneto-elastic systems.

Here, we study the snap-through of elastic bistable beams under magnetic actuation, combining theory, FEM and experiments. First, we demonstrate that snap buckling can be triggered in the presence of an external uniform magnetic field. We quantify how the critical field strength required for buckling depends on the imposed end-to-end shortening (setting the pre-buckled configuration), the beam geometry and the material and magnetization properties. A centreline-based theory is developed to rationalize the trade-offs between the various loading and geometric parameters, predicting the conditions for the onset of snapping. In parallel, we adapt the FEM for three-dimensional h-MREs proposed in [63] to make it amenable to Riks (arc length) analysis. With this enhancement, it is possible to track the stable and unstable branches of the load–displacement curve during snapping. We also probe the beam's load-bearing capacity when the external loading combines a constant magnetic field and poking force.

Our paper is organized as follows. In §2, we define the problem at hand. In §3, we present the experimental method to fabricate the h-MRE beam specimens and describe the experimental protocol for snap buckling tests. The FEM simulations using the Riks method are detailed in §4. In §5, we derive a one-dimensional reduced-order model for bistable magnetic beams. Then, in §§6–8 we report the experimental results and their comparisons with the theoretical and FEM predictions. Finally, our main contributions and an outlook for future work are summarized and discussed in §9.

2. Definition of the problem

We seek to investigate the snap buckling of a bistable magneto-active beam under magnetic loading, which may also be combined with a poking force. We consider a hard-magnetic, thin, elastic beam of length L and rectangular cross-section of width b and thickness h (figure 1*a*). The beam is made of an isotropic and homogeneous h-MRE material with Young's modulus, E, and Poisson's ratio, ν. The configuration of the beam is described using the Cartesian basis vectors

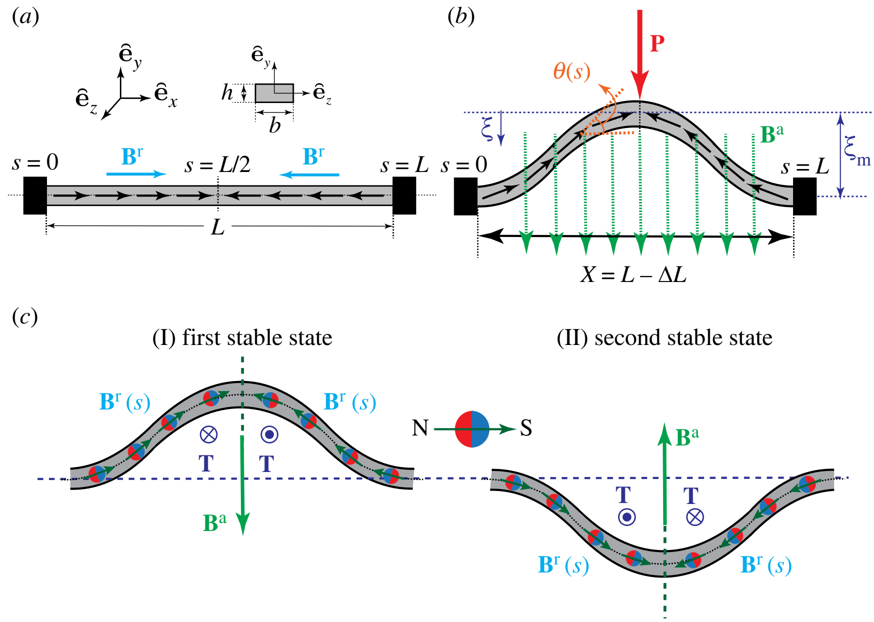

Figure 1. Definition of the problem. (*a*) Schematic diagram of the undeformed configuration of a naturally straight beam of initial length L, thickness h and width b. The beam is composed of two segments with antiparallel magnetization, $\mathbf{B}^r$, along the centreline according to equation (2.1). (*b*) The beam is first pre-loaded by imposing a dimensional end-to-end shortening, ΔL, thereby deforming to a curved, bistable configuration, and then made to snap between the two stable configurations under an applied uniform magnetic field, $\mathbf{B}^a$, and/or an poking force, $\mathbf{P}$. (*c*) The beam exhibits two stable equilibrium states; upon the application of an external magnetic field, the generated torques can switch the beam between configurations (I) and (II). (Online version in colour.)

$(\hat{\mathbf{e}}_x, \hat{\mathbf{e}}_y, \hat{\mathbf{e}}_z)$, aligned, respectively, to the length, thickness and width directions of the originally straight beam (figure 1*a*). The beam is parameterized using the arc length coordinate, $0 \le s \le L$, along its centreline.

The left and right halves of the beam are magnetized permanently in opposite directions, parallel and antiparallel to $\hat{\mathbf{e}}_x$, respectively, with the absolute residual magnetic flux density of B^r (figure 1*a*). Given the slenderness of the beam, the residual magnetic flux density is assumed constant across the cross-section but varies along the arc length direction as

$$\mathbf{B}^r(s) = -B^r \mathrm{sgn}\left(s - \frac{L}{2}\right)\hat{\mathbf{e}}_x. \tag{2.1}$$

Having also compared this magnetization profile with the uniform case, $\mathbf{B}^r = -B^r\hat{\mathbf{e}}_x$, we found that the profile in equation (2.1) is more effective in inducing snap buckling. Even if we recognize that the present choice is ad hoc, it works and it is simple; we leave a more systematic exploration of other magnetization profiles for future work. The magnetic loading is exerted on the beam by the application of an external magnetic field, $\mathbf{B}^a$. Owing to the profile of the residual magnetic flux density vector, $\mathbf{B}^r$, with respect to the direction of the applied magnetic field, $\mathbf{B}^a$, we will demonstrate that the proposed configuration can induce snap-through buckling of the beam.

The magnetized beam is naturally straight in its initial configuration, with the two ends clamped at $s=0$ and $s=L$ (figure 1*a*). To form a buckled (bistable) beam, we then impose a dimensional end-to-end shortening, ΔL, by translating the end at $s=L$ (figure 1*b*), such that the projected length of the beam becomes $X = L - \Delta L$. The (dimensionless) end-to-end shortening is then defined as $\epsilon = \Delta L/L$. In the initial curved configuration set by ϵ with the first-buckling-mode shape, considering w as the displacement of the beam in the $\hat{\mathbf{e}}_y$ direction, the vertical rise of the beam's mid-span along $\hat{\mathbf{e}}_y$, is denoted by ξ_m. Subsequently, the mid-span displacement $w(s = L/2) = \xi \neq \xi_\mathrm{m}$ will vary when external loads are applied. The deformed configuration of the beam is described by the angle, $\theta(s)$, between the tangent of the centreline and $\hat{\mathbf{e}}_x$ (figure 1*b*), with clamped boundaries; $\theta(0) = \theta(L) = 0$.

Once pre-loaded into a curved configuration, the beam can undergo a snap-through instability by the application of either a poking force, $\mathbf{P}$, or a uniform magnetic field, $\mathbf{B}^\mathrm{a}$, or the combination of the two (figure 1*b*). Specifically, under an external magnetic field, a magnetic body torque, $\mathbf{T}$, results from the resistance to rotation of the vector of the residual magnetic flux density, $\mathbf{B}^\mathrm{r}$, which tends to align $\mathbf{B}^\mathrm{r}$ with the applied magnetic field, $\mathbf{B}^\mathrm{a}$ (figure 1*c*). Hence, snap buckling is primarily driven by the magnetic body torque [63]

$$\mathbf{T} = \frac{1}{\mu_0}\mathbf{B}^\mathrm{r} \times \mathbf{B}^\mathrm{a}, \tag{2.2}$$

where μ_0 is the vacuum permeability. Snap buckling can occur under a uniform magnetic field due to the rotation of two halves of the beam in opposite directions. Maximal torque is generated when the magnetic field and the magnetization direction are perpendicular. Thus, the magnetization profile proposed in equation (2.1) lowers the energy barrier required to reach the second stable state. Experimentally, the simplest and closest layout to this configuration can be produced by mid-folding the beam during magnetization, yielding opposite magnetization vectors in each of its halves after unfolding. After switching from one stable state (figure 1*c*I) to another (figure 1*c*II), and removing the exterior magnetic field, the beam stays in the second stable position. The process can be reversed by applying a magnetic field with opposite polarity. In the case of snap buckling under simultaneous mechanical and magnetic loading, the beam is first loaded under a prescribed value of the uniform magnetic field and then indented by a concentrated load applied, $\mathbf{P} = -P\hat{\mathbf{e}}_y$ at its mid-span (figure 1*b*).

Whereas many previous studies have addressed the critical conditions for the classic problem of snap buckling of elastic bistable beams [14,15,33,34,44,74–76], in this study, we investigate the conditions for snapping of a bistable, hard-magnetic beam under the combined influence of the magnetic loading and a poking force.

3. Experimental methods

This section presents the experimental methodology, first, describing the fabrication of the beam specimens (§3a) and, then, detailing the experimental apparatus (§3b). Finally, we describe the experimental protocols, parameters and procedures (§3c).

(a) Fabrication of the beam specimens

The beam specimens were fabricated using a casting protocol adopted from our recent work [65]. The main modification from our previous work is the process we use to magnetize the specimens, with two symmetric regions of antiparallel magnetization. This specific magnetization profile was chosen to facilitate snapping under magnetic loading. Still, for completeness, we provide an overview of the full fabrication protocol.

The beam specimens were cast with an h-MRE, prepared by mixing NdPrFeB particles (average diameter of $5\,\mu\mathrm{m}$, mass density of $\rho_\mathrm{mag} = 7.61\,\mathrm{g\,cm^{-3}}$, MQFP-15-7-20065-089, Magnequench) with vinylpolysiloxane (VPS) polymer (VPS-22, mass density of $\rho_\mathrm{vps} = 1.16\,\mathrm{g\,cm^{-3}}$, Elite Double, Zhermack). The fraction of NdPrFeB particles in the h-MRE was 50.0% in mass ($c_v = 13.2\%$ volume fraction). The mixed solution was injected into a sandwich mould using a syringe to cast a straight beam. Upon curing of the h-MRE, the average Young's modulus was $E = 1.16 \pm 0.04\,\mathrm{MPa}$, the density was $\rho = 2.01 \pm 0.05\,\mathrm{g\,cm^{-3}}$ and the Poisson's ratio was assumed to be $\nu \approx 0.5$ (near incompressibility).

To achieve the desired magnetization profile, we folded the beam at mid-span (figure 2*a*) and placed it inside an impulse magnetizer (IM-K-010020-A, flux density ≈4.4 T, Magnet-Physik

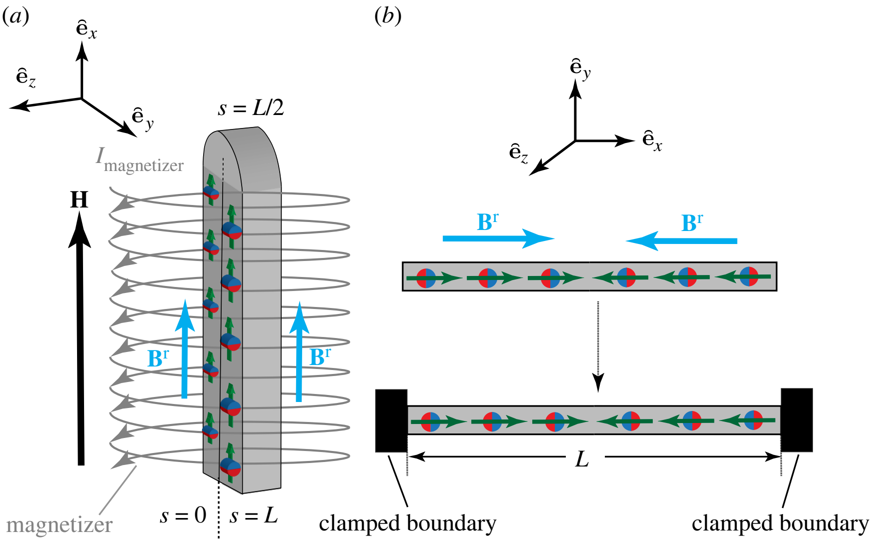

Figure 2. Magnetization of the beam specimen. (*a*) The beam was magnetized while folded at the mid-span, $s = L/2$, inside a pulse magnetizer, which generates a strong axial magnetic field, **H**. (*b*) After unfolding, the magnetized specimen exhibited the antiparallel residual magnetic flux density of $\mathbf{B}^\mathrm{r}$ described in equation (2.1). Two non-magnetic cubic blocks attached to the extremities ensured clamped boundary conditions. (Online version in colour.)

Dr Steingroever GmbH). The magnetization of the embedded particles became permanently aligned to the direction of the field generated by the magnetizer (figure 2*a*). Owing to this folded configuration, after unfolding each half of the beam developed antiparallel magnetization (figure 2*b*), with the residual magnetic flux density, $\mathbf{B}^\mathrm{r}$, described in equation (2.1). Assuming a uniform dispersion of the particles in the polymer matrix, and no re-arrangements during magnetization, the composite can be considered as a homogeneous continuum solid with a uniform magnetization on each half, whose magnitude was computed as the volume-average of the total magnetic moment of the individual particles, $M = 94.1\,\mathrm{kA\,m^{-1}}$.

After magnetization, two non-magnetic cubes of pure VPS ($8 \times 15 \times 15\,\mathrm{mm}^3$) were mounted onto each of the beam extremities to set clamped boundary conditions (figure 2*b*). Finally, the end-to-end shortening, $\epsilon = \Delta L/L$, was imposed on the originally straight beam using an acrylic sample holder, exciting in the first-buckling mode, with bistability, shown schematically in figure 1.

(b) Experimental apparatus

With the originally straight beam set in a curved (bistable) configuration, the experiments involved loading the specimen magnetically, or mechanically, or both, using the apparatus shown in figure 3*a*. Gravitational effects were minimized by placing the beam with the deflection direction, $\hat{\mathbf{e}}_y$, perpendicular to gravity, $-g\hat{\mathbf{e}}_z$. A digital camera was set underneath the coils for imaging (figure 3*a*6).

For the magnetic loading tests, we used a pair of identical coaxial coils (different from the impulse magnetizer mentioned above), in a Helmholtz configuration, which generated a steady axial symmetric magnetic flux density, $\mathbf{B}^\mathrm{a}(x, y, z)$ [70]. The coils were connected in series and separated axially by a distance equal to the mean radius of each coil ($R = 59.5\,\mathrm{mm}$). In this configuration, the current was made to flow through both coils in the same direction to generate a uniform magnetic field in their central region (figure 3*a*),

$$\mathbf{B}^\mathrm{a} = B^\mathrm{a}\hat{\mathbf{e}}_y. \tag{3.1}$$

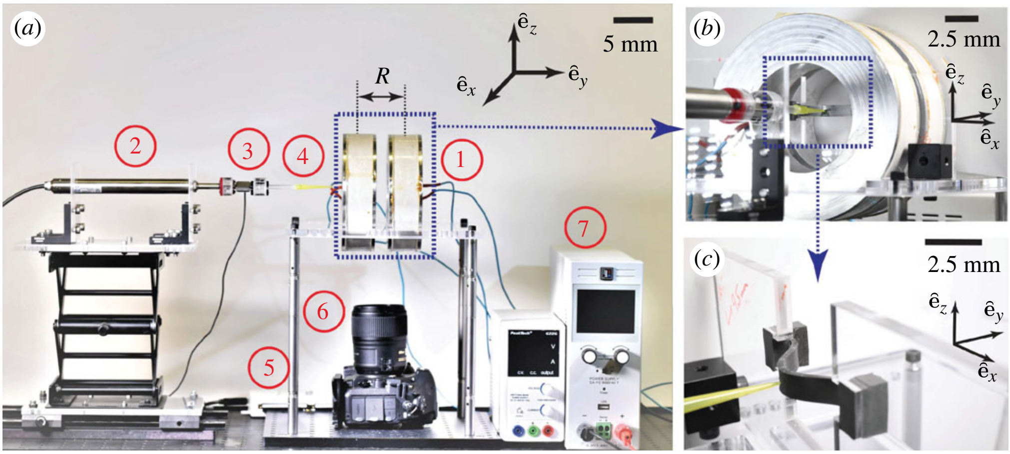

Figure 3. Photographs of the experimental apparatus. (*a*) A magnetic beam is positioned in between a set of Helmholtz coils (1) and loaded by an indenter (4). This indenter is attached to a motorized linear actuator (2), and the reaction force is monitored by a force sensor (3). The force–displacement data is acquired using a LabVIEW data acquisition card (5) and a camera (6) is used to image the beam profile. The coils are driven by the current output of a DC power supplier (7). (*b*) Zoomed view of the pair of Helmholtz coils. (*c*) Representative beam specimen positioned inside the coils. (Online version in colour.)

Each coil was manufactured by winding an aluminium circular spool with an enamelled copper wire (Repelec Moteurs S.A.). The dimensions of the coils were 86 mm for the inner diameter, 152 mm for the outer diameter and 43 mm in height. A DC power supply powered the coils, providing a maximum power of 1.5 kW (EA-PSI 9200-25T, EA-Elektro-Automatik GmbH). The magnitude of the magnetic field, B^{a}, was varied by adjusting the current output (0–25 A) from the power supplier.

For the mechanical load tests, we indented the beam specimen using a custom-built apparatus and measured the force–displacement curves. The poking device comprised two parts: a high-resolution linear actuator (L-220.50DG, PI, Germany) driven by a one-axis DC motor controller (C-863 Mercury Servo Controller, PI, Germany, figure 3*a*2) to impose the displacement, and a force sensor (LRM200, 5lb, JR S-beam load cell, Futek, CA, USA, figure 3*a*3) to measure the reaction force at an acquisition rate of 1 kHz. The indenter was a plastic (non-magnetic) needle cap (plastic taper tip Luer Lock 20GA × 1/4″ Vita needle, MA, USA), chosen to avoid any magnetic field distortions. This indenter assumed rigid compared to the beam specimen was attached to the tip of linear actuator, as shown in figure 3*a*4. The tip of the indenter was glued to the beam at mid-span using VPS solution, thereby restraining rotation and translation at the point of contact. This attachment enabled the acquisition of the complete load–displacement during poking, including both stable and unstable paths.

(c) Experimental protocols

To investigate the snap buckling of bistable hard magnetic beams, we performed three sets of experiments with different loading conditions (i) poking force, (ii) magnetic load and (iii) combined mechanical and magnetic load using, respectively, the poking apparatus, the coils or both. The corresponding results from these experiments will be presented in §§6, 7 and 8, respectively. Next, we detail the configurations of the fabricated specimens, the range of parameters explored and the experimental protocols.

We tested three separate, but otherwise identical, beams (length $L = 60.00 \pm 0.10$ mm, width $b = 8.00 \pm 0.04$ mm and thickness $h = 2.00 \pm 0.06$ mm) to examine the experimental reproducibility and uncertainty. Throughout the experiments, the slenderness ratio was kept constant, $k = L/h = 30$. The end-to-end shortening was varied in the range $0 \le \epsilon =$

$\Delta L/L \le 0.6$. Next, we describe each of the experimental tests, under the different loading conditions.

(i) *Snap-through under poking force*: In order to capture the stable and unstable portions of the loading path, poking force, in the absence of a magnetic field was applied along $\hat{\mathbf{e}}_y$, with the indenter glued to the beam at mid-span ($s = L/2$), and at the constant velocity of $0.02\,\mathrm{mm\,s^{-1}}$ to ensured quasi-static conditions. For each level of ϵ, the mid-span displacement varied in the range $0 \le \xi \le 2\xi_{\mathrm{m}}$.

(ii) *Snap-through under magnetic loading*: In a second set of experiments, the beam specimen was placed within the region of a uniform magnetic field generated by the Helmholtz coils [65]. Two different protocols were followed to measure (ii.a) the critical magnetic field for snapping, $B^{\mathrm{a}}_{\mathrm{cr}}$, and (ii.b) the full load–displacement response, $B^{\mathrm{a}}(\xi)$, as detailed next. To measure $B^{\mathrm{a}}_{\mathrm{cr}}$, we gradually increased the magnitude of the applied magnetic flux density (by increasing the current, I, in the coils; steps of 0.05 A and 10 s) until snap-through occurred. Assuming the snap-through phenomenon is nearly instantaneous, and the waiting time between each two step is larger than the viscous relaxation time [77,78], we neglected dynamic effects and measured the critical snapping magnetic field at the snapping step. (ii.b) By adapting the above experimental procedure, we characterized the full bistable response, capturing the stable and unstable paths. First, prior to magnetic loading, the poking was performed under displacement-control conditions at the speed of $0.02\,\mathrm{mm\,s^{-1}}$ (along $\hat{\mathbf{e}}_y$). The indenter was then stopped at each step of 0.2 mm, and the magnetic field was increased from zero, in the $-\hat{\mathbf{e}}_y$ direction, to balance the poking force, until a zero-force was measured by the load cell. Assuming equilibrium of the specimen and the quasi-static experimental conditions, the measured applied magnetic field required for zero-force was ensured to lie on the equilibrium curve, $B^{\mathrm{a}}(\xi)$.

(iii) *Snap-through under combined mechanical and magnetic load*: In a third set of experiments, we investigated the effect of magnetic loading on the snap-through response of the beam under simultaneous poking force. In each experimental run, the beam was first loaded under a steady magnetic field and then indented following the same protocol as in (i). We repeated the experiment at 11 different levels of magnetic field strength, in the range $-4.5\,\mathrm{mT} \le \mathbf{B}^{\mathrm{a}} \le 53.4\,\mathrm{mT}$, in steps of 6 mT, ensuring that $B^{\mathrm{a}}_{\mathrm{cr}} \le B^{\mathrm{a}}$. From the measured curves of poking force versus displacement, $P(\xi)$, we characterized the stability of the beam for these combined loading conditions.

4. Numerical simulations using FEM

In parallel with the experiments, we performed three-dimensional FEM simulations using an existing user-defined element [63] in the commercial software package ABAQUS/Standard 6.14. As detailed in §4a, we have modified this user element to enable Riks analysis on hard-magnetic structures. The Riks algorithm allows for the solution of the equilibrium equation of a structure by prescribing the arc length of its loading path, so as to track both stable and unstable equilibrium states. We use this technique to study the snapping behaviour of our magnetic beam subjected to a uniform magnetic field. The simulation procedure is, then, detailed in §4b.

(a) User element for Riks analysis

Our FEM approach is based on an existing continuum theory of ideal hard-magnetic soft materials [63] with a permanent magnetization independent of external magnetic fields. In this theory, the effect of an applied magnetic field on a magnetized, deformable body is considered through a potential (density) as a function of the deformation gradient ($\mathbf{F}$), the external field flux density ($\mathbf{B}^{\mathrm{a}}$) and the magnetization of the material (${\mu_0}^{-1}\mathbf{B}^{\mathrm{r}}$):

$$\hat{U}^{\mathrm{m}} = {\mu_0}^{-1}\mathbf{F}\mathbf{B}^{\mathrm{r}} \cdot \mathbf{B}^{\mathrm{a}}. \tag{4.1}$$

This magnetic potential is added to the total energy of the system. Under this description, distributed magnetic torques imposed by the applied field result in an asymmetric part of the Cauchy stress. The field produced by the magnetic body and the induced self-interactions are neglected. This theory has been previously implemented in the commercial FEM software package ABAQUS through a user-defined 8-node solid element [63], while assuming that the elastic behaviour of the material is assumed to be neo-Hookean.

To capture the unstable equilibrium path of the snapping beam under magnetic actuation, we had to adapt this previously developed user element to make it compatible with the Riks analysis in ABAQUS. In the Riks analysis, the magnitude of external loads, which is usually prescribed during a simulation, is considered as an unknown and solved simultaneously with displacements from equilibrium. Alternatively, the 'arc length' of the static equilibrium path of a system in the load–displacement space is imposed to control the progress of the simulation. In order to implement the Riks analysis in the presence of a uniform magnetic field, we define its magnitude as a loading parameter using the keyword `*DLOAD` in ABAQUS, rather than a field variable in the previous work [63]. As such, the field strength can be taken into account as an unknown in the solution domain. This modification on the original user element allows us to simulate both the stable and unstable response of the magnetic beam during snapping, the results of which will be presented in §7.

(b) Simulation procedure

We modelled an initially straight clamped–clamped beam as a three-dimensional solid body. Similarly to the experiments (see figure 2), the beam was composed of two halves with antiparallel magnetization vectors. The length and width of the beam were the same as the experimental specimens. The beam was discretized by the user-defined elements introduced in §4a, using a structured mesh with 16, 4 and 120 elements seeded, respectively, in the width, thickness and length directions. The mesh was deemed to be sufficiently fine through a convergence study. The material of the beam was assumed to be incompressible with a shear modulus $G = 0.39$ MPa (paralleling the experiments; see §3) and a bulk modulus 100 times larger than G. Given the large deflection of the beam during snapping, geometric nonlinearities were taken into account throughout the simulations. We highlight that the simulations employed the material properties characterized in the experiments (see §3), with no fitting parameters.

For the simulation protocol, we first imposed an end-to-end shortening, ϵ, to buckle the beam and reach the preset bistable state. We then studied the snapping of the beam in three loading cases: (i) poking force, (ii) pure magnetic load and (iii) combined mechanical and magnetic loads. Each simulation run involved the following two sequential steps:

Step (a)—Buckling: First, ϵ was imposed to the straight beam, causing it to buckle into a curved configuration characterized by the classic sinusoidal Euler mode for a clamped–clamped beam. In this step, we obtained several post-buckled beam configurations by varying the end-to-end shortening $0 \le \epsilon \le 0.6$; the same range as in the experiments. To trigger buckling, geometric imperfections with the shape of the first eigenmode and a maximum amplitude of $0.1h$ were injected into the initial straight configuration.

Step (b)—Snapping: For loading case (i)—(snap-through under poking force), we indented the beam at mid-span by prescribing the displacement, ξ, which was increased step-by-step until the beam reached the other stable configuration. The poking force, P, was computed as a reaction force from equilibrium. From the load–displacement curve, $P(\xi)$, we identified the critical load for snapping at different end-to-end shortenings (§6). *For loading case (ii)—(snap-through under pure magnetic load)*, we applied a magnetic field on the entire beam with a Riks step, in order to capture the full loading path during snapping. In the search for the equilibrium state, the strength of the applied field is set as an unknown, which, along with the displacements of the beam, was solved under a prescribed arc length increment of the loading path. We computed the critical field strength, the equilibrium path with stable and unstable branches, and the change of the strain energy during snapping. *For loading case (iii)—(snap-through under combined mechanical and magnetic loads)*, a magnetic field with a given flux density lower than the critical value to trigger the snapping was first applied on the beam. Under this constant field, in the next step, we indented the beam by applying a displacement load at the mid-span to make it snap to the other stable configuration. We computed the poking force–displacement curve, $P(\xi)$, for different values of the magnetic field. Then, we extracted the critical poking force under the effect of magnetic load at different end-to-end shortenings.

5. A reduced-order model for the snapping of magnetic beams

We proceed by presenting a centreline-based theory for the problem defined in §2 (see figure 1*b*). We consider a thin, inextensible, hard-magnetic and doubly clamped beam, under Kirchhoff assumptions [79]; i.e. normals to the beam centreline remain normal and unstretched during deformation. Building upon recent developments for hard-magnetic beams [58,59,65,66,80], we develop a one-dimensional beam model through dimensional reduction [81], taking the three-dimensional Helmholtz free energy for ideal hard-magnetic soft materials from Zhao *et al.* [63] as a starting point, on top of other classic ingredients. The elastic (bending) energy of the beam is described by Euler's elastica [81], and the work of poking force was addressed in [75]. Using the principle of virtual work (PVW), we will show that the derived ordinary differential equation (ODE) for the bending angle, $\theta(s)$, is equivalent to a clamped–clamped elastica under a *redefined* poking force applied at mid-span ($s = L/2$). Hence, the effect of the applied magnetic load on the snap-through buckling is qualitatively identical to that of a poking force at mid-span.

Following classic beam kinematics, we define $0 \le s \le L$ to be the arc length of the (inextensible) centreline of a beam, located at $\mathbf{r}(s) = (x(s), y(s))$. We consider a beam clamped both at $s = 0$ and $s = L$, with $\mathbf{r}(0) = (0, 0)$ and $\mathbf{r}(L) = (X, 0)$. The bending angle, $\theta(s)$, is measured from $\hat{\mathbf{e}}_x$, such that the centreline tangent is $\hat{\mathbf{t}} \equiv \mathbf{r}' = (\cos\theta(s), \sin\theta(s))$, where $(\cdot)' = \mathrm{d}(\cdot)/\mathrm{d}s$ and the corresponding boundary conditions are $\theta(0) = \theta(L) = 0$. The relation between $\theta(s)$ and $\mathbf{r}(s)$ is obtained by integrating $\hat{\mathbf{t}}$:

$$\mathbf{r}(L) = (x(L),\ y(L)) = \left(\int_0^L \cos\theta(s)\,\mathrm{d}s,\quad \int_0^L \sin\theta(s)\,\mathrm{d}s\right) = (X,\ 0), \tag{5.1}$$

which acts as a constraint.

Next, we consider first the external virtual work (EVW) and then the internal virtual work (IVW), before invoking the PVW to derive the governing equation for $\theta(s)$.

A reaction force $(F_x,\ F_y)$ is applied at $s = 0$ and the poking force, $\mathbf{P} = (0,\ -P)$, at $s = L/2$. Defining $\mathbf{N}(s) = (N_x, N_y)$ as the internal force on the cross-section at s, force balance yields

$$\mathbf{N}(s) = (N_x, N_y) = \left(-F_x, -F_y + P\Theta\left(s - \frac{L}{2}\right)\right), \tag{5.2}$$

with the Heaviside step function $\Theta(x) = \{\mathrm{sgn}(x) + 1\}/2$ representing the discontinuity (of magnitude P) in the N_y component at $s = L/2$, due to the applied poking force. The EVW is then computed as

$$\mathrm{EVW} = \int_0^L \left\{-F_x\cos\theta + \left(-F_y + P\Theta\left(s - \frac{L}{2}\right)\right)\sin\theta\right\}\,\mathrm{d}s. \tag{5.3}$$

The Helmholtz free energy proposed in [63] for hard-magnetic materials can be decomposed into an elastic part, associated with mechanical deformation, and a magnetic part, arising from the interactions between remanent magnetization and the external field. Based on this decomposition, the total energy of a hard-magnetic beam is the sum of the elastic energy, U^{el}, and the magnetic potential, U^{m}. Assuming a Hookean constitutive law,

$$U^{\mathrm{el}} = \int_0^L \frac{EI}{2} \theta'^2 \, \mathrm{d}s, \tag{5.4}$$

where EI is the flexural rigidity of the beam of Young's modulus, E, and a second moment of inertia, $I = h^3 b/12$.

According to Zhao *et al.* [63], we now make use of the magnetic potential density $\hat{U}^{\mathrm{m}}$ in equation (4.1). Focusing on the geometry of our problem (see figure 1*b*), we set the applied field to $\mathbf{B}^{\mathrm{a}} = B^{\mathrm{a}} \hat{\mathbf{e}}_y$, and the magnetization vector $\mathbf{M} = \mathbf{B}^{\mathrm{r}}/\mu_0$ exhibiting the specific profile of equation (2.1); in the deformed configuration, $\mathbf{M}$ is parallel to the tangent vector $\hat{\mathbf{t}}$ for $0 \le s \le L/2$ (or antiparallel for $L/2 \le s \le L$). The deformation gradient $\mathring{\mathbf{F}}$ for thin beams has been derived in [58,65,80] as

$$\mathring{\mathbf{F}} = \begin{pmatrix} \cos\theta & -\sin\theta \\ \sin\theta & \cos\theta \end{pmatrix}. \tag{5.5}$$

Hence, the magnetic potential for our beam is

$$U^{\mathrm{m}} = -\int_0^L hb \, \mathring{\mathbf{F}} \mathbf{M} \cdot \mathbf{B}^{\mathrm{a}} \, \mathrm{d}s = \frac{hbB^{\mathrm{r}}B^{\mathrm{a}}}{\mu_0} \int_0^L \mathrm{sgn}\left(s - \frac{L}{2}\right) \sin\theta(s) \, \mathrm{d}s. \tag{5.6}$$

Invoking the PVW, mechanical equilibrium is assured when the EVW is balanced by the IVW $= \delta U^{\mathrm{el}} + \delta U^{\mathrm{m}}$ yielding

$$EI\theta'' + F_x \sin\theta - \tilde{F}_y \cos\theta = -\frac{1}{2}\left(P - \frac{2hbB^{\mathrm{a}}B^{\mathrm{r}}}{\mu_0}\right) \mathrm{sgn}\left(s - \frac{L}{2}\right) \cos\theta, \tag{5.7}$$

with $\tilde{F}_y \equiv F_y - (P/2)$ and boundary conditions $\theta(0) = \theta(L) = 0$. The two unknowns, F_x and F_y, are the Lagrange multipliers associated with the clamped boundary [81] and can be determined through equation (5.1). Note that the term in equation (5.7) involving $2hbB^{\mathrm{a}}B^{\mathrm{r}}/\mu_0$ can be interpreted as a second poking force, in addition to P. Therefore, we can define an effective poking force under the combined mechanical and magnetic loading:

$$P^* \equiv P - \frac{2hbB^{\mathrm{a}}B^{\mathrm{r}}}{\mu_0}. \tag{5.8}$$

Hence, the analysis of snap buckling of the hard-magnetic beam under a uniform magnetic field is simplified by treating the developed magnetic torques as an effective poking force acting at mid-span, noting that these two scenarios share similar boundary conditions. A similar approach was followed in [80] for the deformation of the tip of an elastica under magnetic loading. Now, we use equation (5.8) to rewrite equation (5.7) as

$$EI\theta'' + F_x \sin\theta - \tilde{F}_y \cos\theta = -\frac{P^*}{2} \mathrm{sgn}\left(s - \frac{L}{2}\right) \cos\theta. \tag{5.9}$$

This new ODE is equivalent to a clamped–clamped elastica under poking force P^* applied at $s = L/2$ [14,75]. Under appropriate boundary conditions, $\theta(0) = \theta(L) = 0$, and the constraint in equation (5.1), equation (5.9) defines a boundary value problem that can be solved numerically to predict the classic N-shape snap-through response of a doubly clamped beam [14], but now under combined magnetic loading and poking force. We do so using the solver `bvp5c` in `MATLAB`. Note that all the relevant parameters in this model are characterized experimentally, and there are no fitting parameters. In §§6–8, we will compare the predictions from this magnetic beam model against FEM (developed in §4) and experiments (developed in §3).

(a) Linearized theory with $\epsilon \ll 1$ and $|\theta| \ll 1$

For configurations of the bistable beam with small values of end-to-end shortening ($\epsilon \ll 1$), the deformations are small ($|\theta| \ll 1$) at the onset of snapping. In this limit, with $\sin\theta \simeq \theta$ and $\cos\theta \simeq 1 - (\theta^2/2)$, equation (5.9) simplifies to

$$\theta'' + \overline{F}_x\theta - \overline{\tilde{F}}_y = -\frac{\overline{P}^*}{2}\,\mathrm{sgn}\left(\bar{s} - \frac{1}{2}\right), \tag{5.10}$$

where we have used the following dimensionless variables: $\bar{s} = s/L$, $\overline{F}_x \equiv F_x L^2/EI$, $\overline{\tilde{F}}_y \equiv \tilde{F}_y L^2/EI$ and $\overline{P}^* \equiv PL^2/EI - (2hbB^{\mathrm{a}}/B^{\mathrm{r}}L^2EI\mu_0)$. Expanding equation (5.1) with respect to $|\theta| \ll 1$, the corresponding boundary conditions are

$$\int_0^1 \frac{\theta^2(\bar{s})}{2}\,\mathrm{d}\bar{s} = \epsilon, \quad \text{and} \quad \int_0^1 \theta(\bar{s})\,\mathrm{d}\bar{s} = 0. \tag{5.11}$$

Employing the method of variation of parameters, the solution of equation (5.10) is

$$\theta(\bar{s}) = \frac{\overline{\tilde{F}}_y}{\kappa^2}\varphi_1(\bar{s}) + \frac{\overline{P}^*}{\kappa^2}\varphi_2(\bar{s}), \tag{5.12}$$

where we have introduced the wavenumber $\kappa \equiv \sqrt{\overline{F}_x}$ and the functions φ_1 and φ_2, which are, respectively, symmetric and asymmetric functions with respect to $s = 1/2$, defined in Appendix A. The two unknown parameters, $\kappa = \sqrt{\overline{F}_x}$ and $\overline{\tilde{F}}_y$, are determined using the boundary conditions in equation (5.11) to arrive at

$$\kappa = 9 \quad \text{and} \quad 2\epsilon = \left(\frac{\overline{\tilde{F}}_y}{\kappa^2}\right)^2 c_1 + \left(\frac{\overline{P}^*}{\kappa^2}\right)^2 c_2, \tag{5.13}$$

where $c_1 \equiv \int_0^1 (\varphi_1(\bar{s}))^2\,\mathrm{d}\bar{s}$ and $c_2 \equiv \int_0^1 (\varphi_2(\bar{s}))^2\,\mathrm{d}\bar{s}$ are two positive numerical constants detailed in A.

Using equations (5.13), we can now discuss the critical condition for snap buckling. Given that c_1, c_2 and ϵ are all positive, $\overline{\tilde{F}}_y$ ceases to exist, and the beam snaps, when $(\overline{P}^*/\kappa^2)^2 c_2 \geq 2\epsilon$. Hence, the critical condition for the snap transition is

$$|\overline{P}^*_{\mathrm{cr}}| = \kappa^2\sqrt{\frac{2}{c_2}\epsilon} = C_0\sqrt{\epsilon}, \tag{5.14}$$

with the positive constant $C_0 \simeq 130$ [14,75]. The dimensional version of equation (5.14), through equation (5.8), is

$$\left|\frac{bhB^{\mathrm{a}}B^{\mathrm{r}}L^2}{\mu_0 EI} - \frac{P_{\mathrm{cr}}L^2}{2EI}\right| = C_0\sqrt{\epsilon}. \tag{5.15}$$

For reasons that will become clearer in §8, we recognize the critical load at which snapping occurs as the maximum load that the beam can support before snap-through, $P_{\mathrm{cr}} = P_{\mathrm{max}}$, and we rewrite equation (5.15) back in dimensionless form

$$\overline{P}_{\mathrm{max}} = 2(\overline{B}^{\mathrm{a}} + C_0\sqrt{\epsilon}), \tag{5.16}$$

where $\overline{P}_{\mathrm{max}} = P_{\mathrm{max}}L^2/(EI)$ and the applied magnetic field was non-dimensionalized as

$$\overline{B}^a = \frac{bhL^2B^{\mathrm{a}}_{\mathrm{cr}}B^{\mathrm{r}}}{EI\mu_0}, \tag{5.17}$$

characterizing the relative importance between the magnetic load and beam-bending effects. According to equation (5.16), under the assumption of $\epsilon \ll 1$ and when $\overline{B}^a > 0$ (i.e. $\mathbf{B}^{\mathrm{a}}$ and $\mathbf{P}$ are in the same direction), the maximum poking force that the clamped–clamped magnetic beam can support before snapping is expected to depend linearly on the applied magnetic field $\overline{B}^a$, with a slope 2 and an offset $2C_0\sqrt{\epsilon}$ set by the end-to-end shortening. This prediction will be tested

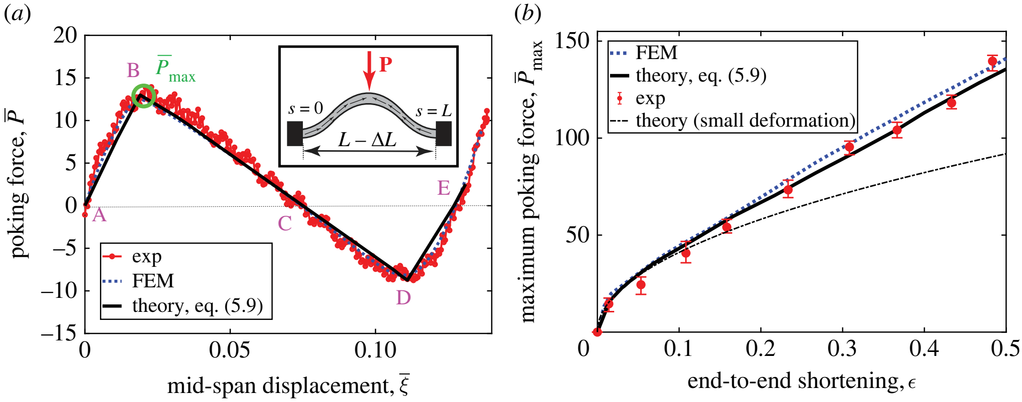

Figure 4. Snap buckling under poking force ($B^a = 0$). (*a*) Normalized poking force, $\overline{P}$, versus the mid-span displacement, $\overline{\xi}$, for the end-to-end shortening of $\epsilon = 0.014$. The maximum of the curve is defined as $\overline{P}_{max}$. (*b*) Normalized maximum poking force, $\overline{P}_{max}$, versus ϵ. The error bars correspond to the standard deviations of the experimental measurements for three identical specimens. (Inset) Schematic diagram of the loading configuration. (Online version in colour.)

against experiments and FEM in figure 8 (§8). In the absence of a magnetic field ($\overline{B}^a = 0$), we recover the standard result, the critical poking force for purely elastic snapping [75], with the scaling $\overline{P}_{max} \sim \sqrt{\epsilon}$, which will be tested against experiments and FEM in figure 4 (in §6).

6. Snapping under poking force

We start by focusing on the classic bistable response when the beam is subjected *only* to a poking force ($B^a = 0$) at mid-span. Even if well-established [75], this case serves as a pre-validation of the framework against experiment, before introducing magnetic effects in §7. In figure 4*a*, we present the results for the dimensionless poking force, $\overline{P} = PL^2/EI$, versus the dimensionless mid-span displacement, $\overline{\xi} = \xi/L$. The initial buckled configuration was generated with an end-to-end shortening of $\epsilon = 0.014$. Then, $\overline{\xi}$ was gradually increased while measuring the poking force. The resulting $\overline{P}(\overline{\xi})$ force–displacement curve exhibits the classic N-shape representative of bistable mechanisms [14]. Points A and E are the two stable stages. The maximum normalized poking force, $\overline{P}_{max}$, occurs at point B. The unstable branch, with negative stiffness, occurs between points B and D, and point C is the unstable equilibrium state. Excellent agreement is found between experiments, FEM and the solution of equation (5.9).

In figure 4b, we plot $\overline{P}_{max}$, as a function of ϵ, finding a sub-linear dependence. For small values of the end-to-end shortening ($\epsilon \lesssim 0.1$), the observed scaling $\overline{P}_{max} \sim \sqrt{\epsilon}$ (dot-dashed line in figure 4*b*) is consistent with equation (5.16) when $B^a = 0$, obtained from the linearized theory for small deformations. For $\epsilon \gtrsim 0.1$, the linearized theory no longer works, but the nonlinear theory of equation (5.9) with $B^a = 0$ (solid line in figure 4*b*) is in excellent agreement with the FEM and experiments, through the full range of explored ϵ. This agreement between the experiments, FEM and the reduced-order beam model, even if within a classic setting, serves as a first step in validation.

7. Snapping under magnetic loading

We proceed by investigating the buckling of the bistable beam under an external magnetic field, this time with no poking force ($P = 0$), seeking to quantify how the critical magnetic field strength, B^a_{cr}, required for switching between the two stable states, depends on the end-to-end shortening, ϵ.

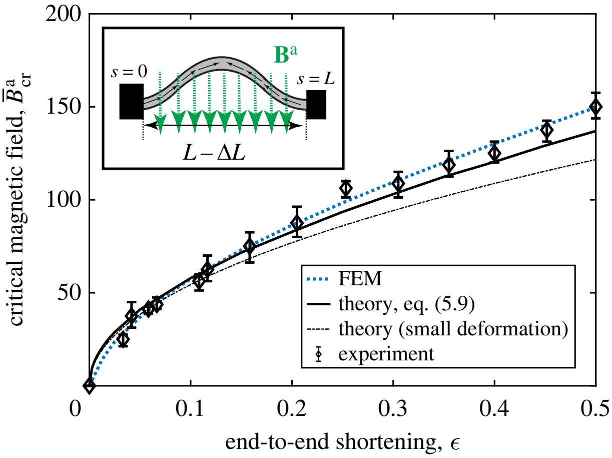

Figure 5. Snap buckling under magnetic actuation. Normalized critical strength of the uniform magnetic field required for beam snapping, $\overline{B}^{a}_{cr}$, as a function of end-to-end shortening, ϵ. The results were obtained from the nonlinear elastic theory in equation (5.9) (solid line), small deformations theory (dashed line), FEM (dotted line) and experiments (data points with error bars). The error bars of the experimental data correspond to the standard deviation of the measurements on three identical specimens. (Inset) Schematic of the bistable beam under magnetic loading. (Online version in colour.)

In figure 5, making use of the dimensionless magneto-elastic parameter defined in equation (5.17), we plot $\overline{B}^{a}_{cr}(\epsilon)$ curves obtained as predicted from FEM simulations, the one-dimensional theory and the experiments. Naturally, increasingly deformed pre-configuration (increasing ϵ) requires a higher value of B^{a}_{cr} for snapping. We find a good agreement between the FEM, the experimental data and the solution of equation (5.9). For small deformations ($\epsilon \lesssim 0.1$), the data follows the scaling $B^{a}_{cr} \sim \sqrt{\epsilon}$, consistently with equation (5.16). For higher values of ϵ, the overall $B^{a}_{cr}(\epsilon)$ curves computed from FEM are captured by the solutions of equation (5.9) with $P = 0$ reasonably well.

The Riks procedure in FEM (cf. §4b) enables us to capture the unstable equilibrium path during snapping under actuation by a magnetic field, from the first to the second stable configuration. In figure 6*a*, we plot the normalized magnetic load, $\overline{B}^{a}$, as a function of the normalized mid-span displacement of the beam, $\overline{\xi}$, for two representative values of the end-to-end shortening, $\epsilon = \{0.008, 0.014\}$. The FEM-computed results (dotted lines) are in quantitative agreement with the experimental data. For $\epsilon = 0.008$, the $\overline{B}^{a}(\overline{\xi})$ curve is non-monotonic, first increasing to a maximum, then decreasing to become negative, until a minimum is reached, to then increase again. The case with $\epsilon = 0.014$ is more complex; the Riks method captures a force–displacement equilibrium path with a complex transition between the two stable states, with winding branches and multiple equilibrium solutions for the same $\overline{\xi}$. However, note that some of the winding-branch segments computed from FEM are not practically relevant; only the solutions with the lowest energy barrier are experimentally observable.

To gain further insight into the energetics of the load–displacement path discussed above, focusing on $\epsilon = 0.014$, we now use FEM to compute the total strain energy, U, as a function of $\overline{\xi}$ during the snapping process; the results are plotted in figure 6*b*. The points A, B, …, G labelled in the plot correspond to the computed configurations shown in figure 6*c*. During the transition path between the stable states A and G, U increases with $\overline{\xi}$ from a minimum (A) to a local maximum (C1) and decreases to another minimum (D). Hence, the corresponding energy barrier, ΔU_s, between this minimum and the local maximum must be overcome for snap-through. According to the principle of minimum potential energy, the lowest energy path is the one observed in practice. Consequently, the higher energy configurations shown in figure 6*c* for points D, C2, E and C3 are not observed experimentally. Indeed, the experimentally observed path in figure 6*a* is an excellent match with the lowest-energy path of figure 6*b*, passing through the points A-B-C1-F-G.

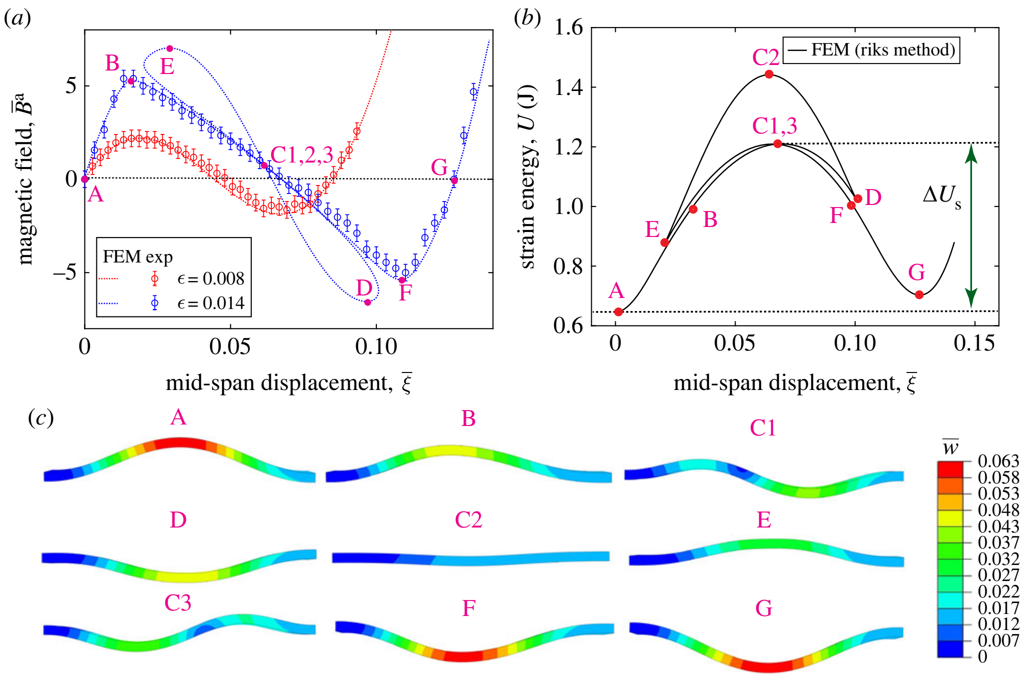

Figure 6. Bifurcation diagram for the snap-through of the bistable beam under magnetic actuation. (*a*) Normalized magnetic field, $\overline{B}^a$, versus the normalized mid-span displacement, $\overline{\xi}$: FEM simulations and experiments for two beams with $\epsilon = \{0.008,\ 0.014\}$. (*b*) FEM-computed strain energy, U, versus $\overline{\xi}$, for $\epsilon = 0.014$. The beam must overcome the energy barrier, ΔU_s (vertical double-arrow), to switch between the two stable states. (*c*) Representative FEM-computed configurations of the beam along the equilibrium solution path, corresponding to the same points in the plots of (*a*) and (*b*). The colour bar represents the normalized displacement of the beam along the *y*-axis, $\overline{w}$. (Online version in colour.)

8. Snapping under combined poking force and magnetic loading

Finally, we turn to the combined case of simultaneously loading the bistable beams with mechanical poking and a magnetic field, each of which was tackled individually in the previous §§6 and 7. We seek to quantify how the magnetic loading modifies the load-bearing capacity of the bistable beam under poking force and characterize the critical conditions for snap buckling.

In figure 7*a*, we present the normalized poking force, $\overline{P}$, versus the beam's mid-span displacement, $\overline{\xi}$, at different levels of the uniform magnetic field, $\overline{B}^a\hat{\mathbf{e}}_y$, varied systematically in the range $-3.9 \le \overline{B}^a \le 46.9$ (see legend of the plot). We focus on the representative case with $\epsilon = 0.014$. To track the full equilibrium path, including its unstable portions, the indenter was glued to the beam at mid-span, as described in §3c. At each value of $\overline{B}^a$, the signal-to-noise ratio of the measurements was enhanced by repeating three independent, but otherwise identical, experimental runs; their average is reported as the $\overline{P}(\overline{\xi})$ curves of figure 7*a*. Throughout, excellent agreement is found between experiments (solid lines) and the FEM (dotted lines).

Under an external magnetic field, the poking force–displacement response of the hard-magnetic beam can be modified significantly with respect to the purely mechanical case ($\overline{B}^a = 0$ and results in §6). When the applied magnetic field is in the opposite direction of the poking force ($\overline{B}^a > 0$), the generated magnetic torques oppose the direction of the poking-induced beam rotation. Consequently, as the field strength is increased, the beam stiffens and becomes more resistant to snap buckling (the local maximum of $\overline{P}$ increases). By contrast, when the magnetic load is applied in the same direction to the poking ($\overline{B}^a < 0$), snap-through occurs at lower poking forces as the magnetic torques are in the same direction as the poking-induced rotation.

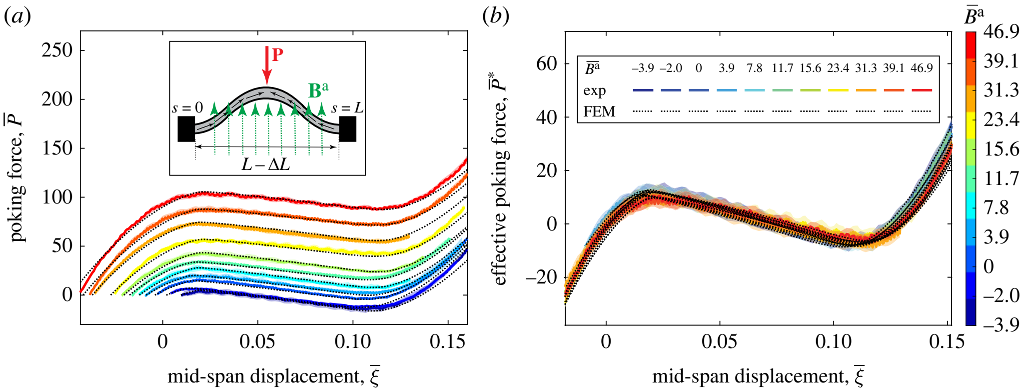

Figure 7. Load–displacement curves for the indented magnetic beam (with $\epsilon = 0.014$) in the presence of a uniform magnetic field. (*a*) The normalized poking force, $\bar{P}$, is plotted versus the normalized mid-span displacement, $\bar{\xi}$, at various levels of prescribed field strength, $\bar{B}^{a}$. (Inset) Schematic diagram of the bistable beam under combined magnetic and mechanical loading. (*b*) The normalized effective poking force, $\bar{P}^*$, as a function of the normalized mid-span displacement, $\bar{\xi}$, for the curves in (*a*), collapsing on a single curve. The experiments and FEM simulations are represented by solid lines, and dotted lines, respectively. The shaded region of each curve represents the standard deviation of three identical measurements. (Online version in colour.)

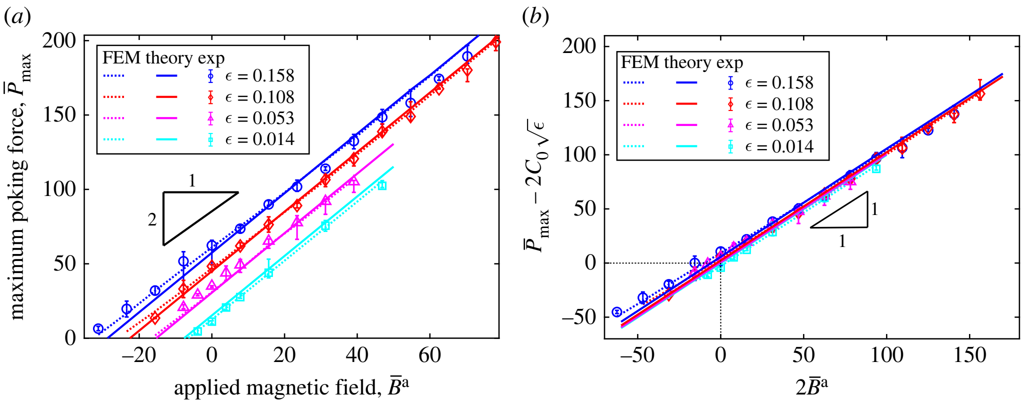

Figure 8. Critical poking force for snap transition under magnetic actuation. (*a*) Normalized maximum poking force, $\bar{P}_{max}$, versus the prescribed applied magnetic field, $\bar{B}^{a}$, at different end-to-end shortenings ($\epsilon = \{0.158, 0.108, 0.053, 0.014\}$): experiments (data points), theoretical predictions from equation (5.9) (solid lines), and FEM (dotted lines). The line slope of 2 is consistent with equation (5.16). (*b*) Master curve for the experimental results, FEM simulations and the theoretical predictions, for the data in (*a*). The quantity, $\bar{P}_{max} - 2C_0\sqrt{\epsilon}$ in equation (5.16), is plotted as a function of $2\bar{B}^{a}$, yielding a collapse of all the data. The term $-2C_0\sqrt{\epsilon}$ removes the offset due to the end-to-end shortening. (Online version in colour.)

In figure 7*b*, to compare the elastic and magnetic loads, we plot the normalized effective poking force, $\bar{P}^*$, as a function of the normalized mid-span displacement, $\bar{\xi}$, for the corresponding curves in figure 7*a*. We find that the experimental and simulations data collapse into a single curve, indicating that the effect of magnetic load on the snap buckling of magnetic beams can be interpreted as a second poking force in addition to the mechanical load (see §5). Treatment of the effect of magnetic torques developed under a uniform magnetic field as an equivalent poking force acting at mid-span simplifies the calculation of the critical snap buckling load for a hard-magnetic beam under combined elastic and magnetic loading.

In figure 8*a*, we quantify the dimensionless relation between the maximum (critical) poking force, $\overline{P}_{\max}$, and the magnitude of the prescribed magnetic field $\overline{B}^{\mathrm{a}}$, for four values of the end-to-end shortenings, $\epsilon = \{0.014, 0.053, 0.108, 0.158\}$. The experimental force–displacement signals were smoothed with a 50-point moving average filter, to facilitate the extraction of $\overline{P}_{\max}$, the largest load that the beam can sustain prior to snapping. Again, an excellent agreement is observed between the experiments (data points), FEM (dotted lines) and the solution of equation (5.9) (solid lines). We find the robust linear scaling $\overline{P}_{\max} \sim \overline{B}^{\mathrm{a}}$, with a slope of 2. Increasing ϵ results in an increase of the offset at $\overline{B}^{\mathrm{a}} = 0$ of the linear curves, as dictated by the purely mechanical poking case in figure 4. Hence, increasing the end-to-end shortening results in a larger poking force required for snapping under a particular level of field strength, set by the offset of the linear behaviour. The experimental and FEM data are in remarkable agreement with equation (5.16), indicating that the largest value of end-to-end shortening explored in these experiments (and FEM simulations) still lies in the regime of validity, with small deformations ($|\theta| \ll 1$), of the linearized theory developed in §5a.

In figure 8*b*, making use of equation (5.16), we now replot all the data in figure 8a but with $\overline{P}_{\max} - 2C_0\sqrt{\epsilon}$ as a function of $2\overline{B}^{\mathrm{a}}$. The purpose is to remove the effect of end-to-end shortening, and characterize the magneto-elastic effect of the snapping beam. Again as predicted by the linearized theory, we find a striking collapse of all the data into a master curve of unit slope, passing through the origin. This collapse indicates that equation (5.16), based on a linearized theory and combining the dimensionless groups of magnetic ($bhB^{\mathrm{a}}B^{\mathrm{r}}L^2/\mu_0 EI$) and mechanical ($PL^2/EI$) loads, serves as a high-fidelity description of the magneto-elastic behaviour of our hard-magnetic bistable beams, with different end-to-end shortenings ($\epsilon \lesssim 0.1$), in the limit of small deformations ($\theta \ll 1$).

9. Conclusion

We investigated the snapping behaviour of bistable magneto-active beams under combined mechanical and magnetic actuation, incorporating experiments, FEM and a reduced-order model. Considering a pre-compressed bistable beam with different levels of end-to-end shortening, we characterized the load–displacement response, the critical poking force, the field strength at the onset of snapping and the effect of magnetic loading on snap buckling under poking force. The Riks method was employed in the three-dimensional FEM simulations to analyse the snap transition. We also developed a beam theory to rationalize the observed magneto-elastic response. Precision experiments validated the theory and the FEM simulations.

More specifically, we studied the snap buckling of the beam under three different loading cases: (i) poking force only, (ii) magnetic field only and (iii) combined magnetic and mechanical loading. Case (i), even if classic, served for pre-validation. In case (ii), we triggered snap buckling under a magnetic field for various end-to-end shortenings, by designing the magnetization profile of the beam. For small-deformations, the critical magnetic field increased with the square root of the end-to-end shortening. The Riks method was used to explore the equilibrium transition path, finding that increasing the end-to-end shortening complicates the instability response, but the experimentally observable solution corresponds to the lowest energy level. Finally, in case (iii), we examined how magnetic loading affects the poking-induced snapping of the bistable beam. The critical poking force for snapping can be adjusted by the magnitude and direction of the magnetic field. Our magnetic beam model captures these results. In the small deformation limit, the critical poking force at the onset of snapping is linearly proportional to the applied magnetic field with a slope and offset that can be predicted. In this limit, a master curve is uncovered that collapses the experimental and FEM-computed data.

Our study provides insight into the nonlinear magneto-elastic coupling of bistable beams, which could be extended in several directions for future work. Fundamentally, the dynamics of multi-stable structures integrated with soft active materials remains relatively unexplored and deserves further attention. From a practical viewpoint, optimization and inverse design is an exciting direction: compact actuators could be designed using bistable beams while minimizing the total energy consumption during actuation. The magnetization profile chosen in equation (2.1) may come across as ad hoc, even if we found that it is more effective in inducing snap buckling compared to uniform magnetization. Future work should explore other magnetization designs more systematically. Owing to the complex relationship between the design parameters and snap-through characteristics, modelling the deformation of bistable beams under other boundary conditions should be considered.

It is important to highlight that a recent study on hard-magnetic plates [69] proposed a rotation-based (**R**-based) magnetic potential by replacing the deformation gradient, **F**, in equation (4.1) with the rotation tensor. This work was, in turn, motivated by an also equally recent, but prior, demonstration of the stretch-independence of the magnetization of bulk h-MREs [64]. Indeed, the subsequent experiments in [69] showed that the **R**-based model is necessary for plates subjected to non-negligible stretching deformation under an applied field parallel to the initial magnetization. These latest findings bring into question why, in the present paper, we decided not to use the **R**-based magnetic potential, choosing the **F**-based model description instead. Given the assumption of inextensible centreline made when developing the beam model, together with the orthogonality between the field and the initial magnetization of the configuration considered in this work, the potential in equation (4.1) is expected to be appropriate for the current problem, as also justified by the excellent agreement between our theory, FEM and experiments. Also, the Kirchhoff assumptions adopted in the one-dimensional model correct the error from using the potential in equation (4.1), as pointed out in [69], given that inextensibility together with the fact that normals do not change length, thereby removing any stretching-induced effects from the **F**-based model. As a final practical justification, the **F**-based model being significantly simpler mathematically than the **R**-based one and, therefore, it is preferable in cases where both yield the same results. Still, future efforts should be dedicated to develop **R**-based beam and rod models for more general cases where stretching of the centreline may be important.

In closing, we believe that our comprehensive framework is a step forward toward the predictive design of bistable magneto-elastic beams. We hope that the snapping behaviour and the stiffness-tuning capability of these components will be exploited for a variety of future applications, including actuators, robotics, MEMS, programmable devices, metamaterials and energy harvesting devices.

Data accessibility. All data relevant to the figures in this manuscript are available as electronic supplementary material.

The data are provided in electronic supplementary material [82].

Authors' contributions. A.A.: conceptualization, data curation, formal analysis, investigation, methodology, software, validation, visualization, writing—original draft, writing—review and editing; T.G.S.: conceptualization, formal analysis, investigation, methodology, software, validation, writing—original draft, writing—review and editing; D.Y.: conceptualization, formal analysis, investigation, methodology, software, validation, writing—original draft, writing—review and editing; P.M.R.: conceptualization, investigation, methodology, supervision, writing—original draft, writing—review and editing.

All authors gave final approval for publication and agreed to be held accountable for the work performed therein.

Conflict of interest declaration. We declare we have no competing interests.

Funding. A.A. is grateful to the support from the Federal Commission for Scholarships for Foreign Students (FCS) through a Swiss Government Excellence Scholarship (grant no. 2019.0619).

Appendix A. Solution of equation (5.10)

Here, we discuss a few details of the solution of equation (5.10) to arrive at equation (5.12). The functions, φ_1 and φ_2, were introduced to solve the linear inhomogeneous ODE with the method of variation of parameters (§8) and are written as

$$\varphi_1(s) \equiv 1 - \frac{\cos\left(\kappa\left(s - \frac{1}{2}\right)\right)}{\cos(\kappa/2)} \tag{A 1}$$

and

$$\varphi_2(s) \equiv \frac{1}{2}\left[\operatorname{sgn}\left(s-\frac{1}{2}\right)\left\{\cos\left(\kappa\left(s-\frac{1}{2}\right)\right)-1\right\}+\tan\left(\frac{\kappa}{4}\right)\sin\left(\kappa\left(s-\frac{1}{2}\right)\right)\right], \tag{A 2}$$

where we have used $\tan(\kappa/4) = (1-\cos(\kappa/2))/\sin(\kappa/2)$. Note that $\varphi_1(s)$ and $\varphi_2(s)$ are, respectively, symmetric and asymmetric function with respect to $s = 1/2$. The two numerical constants in equation (5.13), c_1 and c_2, are computed as

$$\left.\begin{aligned} c_1 &\equiv \int_0^1 \varphi_1^2(s)\mathrm{d}s = \frac{2\kappa - 3\sin\kappa + \kappa\cos\kappa}{\kappa + \kappa\cos\kappa} \\ \text{and} \qquad c_2 &\equiv \int_0^1 \varphi_2^2(s)\,\mathrm{d}s = \frac{1}{8}\left(2 + \frac{1}{\cos^2(\kappa/4)} - \frac{12}{\kappa}\tan\left(\frac{\kappa}{4}\right)\right).\end{aligned}\right\} \tag{A 3}$$

References

1. Singer J, Arbocz J, Weller T. 2002 *Buckling experiments: experimental methods in buckling of thin-walled structures: shells, built-up structures, composites and additional topics*, vol. 2. New York, NY: John Wiley & Sons.
2. Thompson JMT, Sieber J. 2016 Shock-sensitivity in shell-like structures: with simulations of spherical shell buckling. *Int. J. Bifurc. Chaos* **26**, 1630003. (doi:10.1142/S0218127416300032)
3. Thompson JMT. 2015 Advances in shell buckling: theory and experiments. *Int. J. Bifurc. Chaos* **25**, 1530001. (doi:10.1142/S0218127415300013)
4. Thompson JMT, Hutchinson JW, Sieber J. 2017 Probing shells against buckling: a nondestructive technique for laboratory testing. *Int. J. Bifurc. Chaos* **27**, 1730048. (doi:10.1142/S0218127417300488)
5. Virot E, Kreilos T, Schneider TM, Rubinstein SM. 2017 Stability landscape of shell buckling. *Phys. Rev. Lett.* **119**, 224101. (doi:10.1103/PhysRevLett.119.224101)
6. Marthelot J, López Jiménez F, Lee A, Hutchinson JW, Reis PM. 2017 Buckling of a pressurized hemispherical shell subjected to a probing force. *J. Appl. Mech.* **84**, 121005. (doi:10.1115/1.4038063)
7. Abbasi A, Yan D, Reis PM. 2021 Probing the buckling of pressurized spherical shells. *J. Mech. Phys. Solids* **155**, 104545. (doi:10.1016/j.jmps.2021.104545)
8. Bazant ZP, Cedolin L, Hutchinson J. 1993 *Stability of structures: elastic, inelastic, fracture, and damage theories*. New York, NY: Oxford University Press.
9. Cao Y, Derakhshani M, Fang Y, Huang G, Cao C. 2021 Bistable structures for advanced functional systems. *Adv. Funct. Mater.* **31**, 2106231. (doi:10.1002/adfm.202106231)
10. Harne RL, Wang KW. 2017 *Harnessing bistable structural dynamics: for vibration control, energy harvesting and sensing*. New York, NY: John Wiley & Sons.
11. Ghosh A, Koster G, Rijnders G. 2016 Multistability in bistable ferroelectric materials toward adaptive applications. *Adv. Funct. Mater.* **26**, 5748–5756. (doi:10.1002/adfm.201601353)
12. Harne RL, Wang K. 2013 A review of the recent research on vibration energy harvesting via bistable systems. *Smart Mater. Struct.* **22**, 023001. (doi:10.1088/0964-1726/22/2/023001)
13. Sun X, Zhang Y, Kennedy D. 2019 On stochastic dynamic analysis and assessment of bistable structures. *Nonlinear Dyn.* **95**, 3205–3218. (doi:10.1007/s11071-018-04750-4)
14. Vangbo M, Bäcklund Y. 1998 A lateral symmetrically bistable buckled beam. *J. Micromech. Microeng.* **8**, 29. (doi:10.1088/0960-1317/8/1/005)
15. Saif MTA. 2000 On a tunable bistable MEMS-theory and experiment. *J. Microelectromech. Syst.* **9**, 157–170. (doi:10.1109/84.846696)
16. Chen T, Bilal OR, Shea K, Daraio C. 2018 Harnessing bistability for directional propulsion of soft, untethered robots. *Proc. Natl Acad. Sci. USA* **115**, 5698–5702. (doi:10.1073/pnas.1800386115)
17. Rothemund P, Ainla A, Belding L, Preston DJ, Kurihara S, Suo Z, Whitesides GM. 2018 A soft, bistable valve for autonomous control of soft actuators. *Sci. Robot.* **3**, eaar7986. (doi:10.1126/scirobotics.aar7986)
18. Stanton SC, McGehee CC, Mann BP. 2010 Nonlinear dynamics for broadband energy harvesting: investigation of a bistable piezoelectric inertial generator. *Physica D* **239**, 640–653. (doi:10.1016/j.physd.2010.01.019)

19. Clingman DJ, Thiesen J. 2017 The development of two broadband vibration energy harvesters (BVEH) with adaptive conversion electronics. In *Industrial and commercial applications of smart structures technologies 2017*, vol. 10166 (ed DJ Clingman), pp. 68–86. Portland, OR: International Society for Optics and Photonics.
20. Crivaro A, Sheridan R, Frecker M, Simpson TW, Von Lockette P. 2016 Bistable compliant mechanism using magneto active elastomer actuation. *J. Intell. Mater. Syst. Struct.* **27**, 2049–2061. (doi:10.1177/1045389X15620037)
21. Hou X, Liu Y, Wan G, Xu Z, Wen C, Yu H, Zhang JX, Li J, Chen Z. 2018 Magneto-sensitive bistable soft actuators: experiments, simulations, and applications. *Appl. Phys. Lett.* **113**, 221902. (doi:10.1063/1.5062490)
22. Treml B, Gillman A, Buskohl P, Vaia R. 2018 Origami mechanologic. *Proc. Natl Acad. Sci. USA* **115**, 6916–6921. (doi:10.1073/pnas.1805122115)
23. Faber JA, Arrieta AF, Studart AR. 2018 Bioinspired spring origami. *Science* **359**, 1386–1391. (doi:10.1126/science.aap7753)
24. Chen T, Mueller J, Shea K. 2017 Integrated design and simulation of tunable, multi-state structures fabricated monolithically with multi-material 3D printing. *Sci. Rep.* **7**, 45671. (doi:10.1038/srep45671)
25. Liu X, Lamarque F, Doré E, Pouille P. 2015 Multistable wireless micro-actuator based on antagonistic pre-shaped double beams. *Smart Mater. Struct.* **24**, 075028. (doi:10.1088/0964-1726/24/7/075028)
26. Fang W, Wickert J. 1994 Post buckling of micromachined beams. *J. Micromech. Microeng.* **4**, 116. (doi:10.1088/0960-1317/4/3/004)
27. Jeon JH, Cheng TH, Oh IK. 2010 Snap-through dynamics of buckled IPMC actuator. *Sens. Actuators A: Phys.* **158**, 300–305. (doi:10.1016/j.sna.2010.01.030)
28. Cleary J, Su HJ. 2015 Modeling and experimental validation of actuating a bistable buckled beam via moment input. *J. Appl. Mech.* **82**, 051005. (doi:10.1115/1.4030074)
29. Vangbo M. 1998 An analytical analysis of a compressed bistable buckled beam. *Sens. Actuators A: Phys.* **69**, 212–216. (doi:10.1016/S0924-4247(98)00097-1)
30. Yan W, Yu Y, Mehta A. 2019 Analytical modeling for rapid design of bistable buckled beams. *Theor. Appl. Mech. Lett.* **9**, 264–272. (doi:10.1016/j.taml.2019.04.006)
31. Zhao J, Jia J, He X, Wang H. 2008 Post-buckling and snap-through behavior of inclined slender beams. *J. Appl. Mech.* **75**, 041020. (doi:10.1115/1.2870953)
32. Cazottes P, Fernandes A, Pouget J, Hafez M. 2009 Bistable buckled beam: modeling of actuating force and experimental validations. *J. Mech. Des.* **131**, 1001001–1001011. (doi:10.1115/1.3179003)
33. Camescasse B, Fernandes A, Pouget J. 2013 Bistable buckled beam: elastica modeling and analysis of static actuation. *Int. J. Solids Struct.* **50**, 2881–2893. (doi:10.1016/j.ijsolstr.2013.05.005)
34. Camescasse B, Fernandes A, Pouget J. 2014 Bistable buckled beam and force actuation: experimental validations. *Int. J. Solids Struct.* **51**, 1750–1757. (doi:10.1016/j.ijsolstr.2014.01.017)
35. Harvey Jr P, Virgin L. 2015 Coexisting equilibria and stability of a shallow arch: unilateral displacement-control experiments and theory. *Int. J. Solids Struct.* **54**, 1–11. (doi:10.1016/j.ijsolstr.2014.11.016)
36. Cazzolli A, Dal Corso F. 2019 Snapping of elastic strips with controlled ends. *Int. J. Solids Struct.* **162**, 285–303. (doi:10.1016/j.ijsolstr.2018.12.005)
37. Zhang Y, Jiao Y, Wu J, Ma Y, Feng X. 2020 Configurations evolution of a buckled ribbon in response to out-of-plane loading. *Extreme Mech. Lett.* **34**, 100604. (doi:10.1016/j.eml.2019.100604)
38. Wan G, Liu Y, Xu Z, Jin C, Dong L, Han X, Zhang JX, Chen Z. 2020 Tunable bistability of a clamped elastic beam. *Extreme Mech. Lett.* **34**, 100603. (doi:10.1016/j.eml.2019.100603)
39. Plaut RH. 2015 Snap-through of arches and buckled beams under unilateral displacement control. *Int. J. Solids Struct.* **63**, 109–113. (doi:10.1016/j.ijsolstr.2015.02.044)
40. Krylov S, Ilic BR, Lulinsky S. 2011 Bistability of curved microbeams actuated by fringing electrostatic fields. *Nonlinear Dyn.* **66**, 403–426. (doi:10.1007/s11071-011-0038-y)
41. Medina L, Gilat R, Krylov S. 2018 Bistability criterion for electrostatically actuated initially curved micro plates. *Int. J. Eng. Sci.* **130**, 75–92. (doi:10.1016/j.ijengsci.2018.05.006)
42. Maurini C, Pouget J, Vidoli S. 2007 Distributed piezoelectric actuation of a bistable buckled beam. *Eur. J. Mech.-A/Solids* **26**, 837–853. (doi:10.1016/j.euromechsol.2007.02.001)

43. Ramachandran V, Bartlett MD, Wissman J, Majidi C. 2016 Elastic instabilities of a ferroelastomer beam for soft reconfigurable electronics. *Extreme Mech. Lett.* **9**, 282–290. (doi:10.1016/j.eml.2016.08.007)
44. Amor A, Fernandes A, Pouget J. 2020 Snap-through of elastic bistable beam under contactless magnetic actuation. *Int. J. Non-Linear Mech.* **119**, 103358. (doi:10.1016/j.ijnonlinmec.2019.103358)
45. Carlson JD, Jolly MR. 2000 MR fluid, foam and elastomer devices. *Mechatronics* **10**, 555–569. (doi:10.1016/S0957-4158(99)00064-1)
46. Danas K, Kankanala S, Triantafyllidis N. 2012 Experiments and modeling of iron-particle-filled magnetorheological elastomers. *J. Mech. Phys. Solids* **60**, 120–138. (doi:10.1016/j.jmps.2011.09.006)
47. Gray BL. 2014 A review of magnetic composite polymers applied to microfluidic devices. *J. Electrochem. Soc.* **161**, B3173. (doi:10.1149/2.023402jes)
48. Li Y, Li J, Li W, Du H. 2014 A state-of-the-art review on magnetorheological elastomer devices. *Smart Mater. Struct.* **23**, 123001. (doi:10.1088/0964-1726/23/12/123001)
49. Bica I, Anitas EM, Bunoiu M, Vatzulik B, Juganaru I. 2014 Hybrid magnetorheological elastomer: influence of magnetic field and compression pressure on its electrical conductivity. *J. Ind. Eng. Chem.* **20**, 3994–3999. (doi:10.1016/j.jiec.2013.12.102)
50. Hines L, Petersen K, Lum GZ, Sitti M. 2017 Soft actuators for small-scale robotics. *Adv. Mater.* **29**, 1603483. (doi:10.1002/adma.201603483)
51. Kim Y, Yuk H, Zhao R, Chester SA, Zhao X. 2018 Printing ferromagnetic domains for untethered fast-transforming soft materials. *Nature* **558**, 274. (doi:10.1038/s41586-018-0185-0)
52. Hu W, Lum GZ, Mastrangeli M, Sitti M. 2018 Small-scale soft-bodied robot with multimodal locomotion. *Nature* **554**, 81–85. (doi:10.1038/nature25443)
53. Wu S, Hu W, Ze Q, Sitti M, Zhao R. 2020 Multifunctional magnetic soft composites: a review. *Multifunct. Mater.* **3**, 042003. (doi:10.1088/2399-7532/abcb0c)
54. Chen T, Pauly M, Reis PM. 2021 A reprogrammable mechanical metamaterial with stable memory. *Nature* **589**, 386–390. (doi:10.1038/s41586-020-03123-5)
55. Wang L, Zheng D, Harker P, Patel AB, Guo CF, Zhao X. 2021 Evolutionary design of magnetic soft continuum robots. *Proc. Natl Acad. Sci. USA* **118**, e2021922118. (doi:10.1073/pnas.2021922118)
56. Kim Y, Zhao X. 2022 Magnetic soft materials and robots. *Chem. Rev.* **122**, 5317–5364. (doi:10.1021/acs.chemrev.1c00481)
57. Miyazaki T, Jin H. 2012 *The physics of ferromagnetism*, vol. 158. Berlin, Germany: Springer Science & Business Media.
58. Lum GZ, Ye Z, Dong X, Marvi H, Erin O, Hu W, Sitti M. 2016 Shape-programmable magnetic soft matter. *Proc. Natl Acad. Sci. USA* **113**, E6007–E6015. (doi:10.1073/pnas.1608193113)
59. Ciambella J, Tomassetti G. 2020 A form-finding strategy for magneto-elastic actuators. *Int. J. Non-Linear Mech.* **119**, 103297. (doi:10.1016/j.ijnonlinmec.2019.103297)
60. Chen W, Yan Z, Wang L. 2020a Complex transformations of hard-magnetic soft beams by designing residual magnetic flux density. *Soft Matter* **16**, 6379–6388. (doi:10.1039/C9SM02529D)
61. Chen W, Yan Z, Wang L. 2020b On mechanics of functionally graded hard-magnetic soft beams. *Int. J. Eng. Sci.* **157**, 103391. (doi:10.1016/j.ijengsci.2020.103391)
62. Alapan Y, Karacakol AC, Guzelhan SN, Isik I, Sitti M. 2020 Reprogrammable shape morphing of magnetic soft machines. *Sci. Adv.* **6**, eabc6414. (doi:10.1126/sciadv.abc6414)
63. Zhao R, Kim Y, Chester SA, Sharma P, Zhao X. 2019 Mechanics of hard-magnetic soft materials. *J. Mech. Phys. Solids* **124**, 244–263. (doi:10.1016/j.jmps.2018.10.008)
64. Mukherjee D, Rambausek M, Danas K. 2021 An explicit dissipative model for isotropic hard magnetorheological elastomers. *J. Mech. Phys. Solids* **151**, 104361. (doi:10.1016/j.jmps.2021.104361)
65. Yan D, Abbasi A, Reis PM. 2021 A comprehensive framework for hard-magnetic beams: reduced-order theory, 3D simulations, and experiments. *Int. J. Solids Struct.* **257**, 111319. (doi:10.1016/j.ijsolstr.2021.111319)
66. Sano TG, Pezzulla M, Reis PM. 2022 A Kirchhoff-like theory for hard magnetic rods under geometrically nonlinear deformation in three dimensions. *J. Mech. Phys. Solids* **160**, 104739. (doi:10.1016/j.jmps.2021.104739)

67. Sano TG. 2022 Reduced theory for hard magnetic rods with dipole–dipole interactions. *J. Phys. A: Math. Theor.* **55**, 104002. (doi:10.1088/1751-8121/ac4de2)
68. Chen W, Wang L. 2020 Theoretical modeling and exact solution for extreme bending deformation of hard-magnetic soft beams. *J. Appl. Mech.* **87**, 041002. (doi:10.1115/1.4045716)
69. Yan D, Aymon BF, Reis PM. 2023 A reduced-order, rotation-based model for thin hard-magnetic plates. *J. Mech. Phys. Solids* **170**, 105095. (doi:10.1016/j.jmps.2022.105095)
70. Yan D, Pezzulla M, Cruveiller L, Abbasi A, Reis PM. 2021 Magneto-active elastic shells with tunable buckling strength. *Nat. Commun.* **12**, 2831. (doi:10.1038/s41467-021-22776-y)
71. Pezzulla M, Yan D, Reis PM. 2022 A geometrically exact model for thin magneto-elastic shells. *J. Mech. Phys. Solids* **166**, 104916. (doi:10.1016/j.jmps.2022.104916)
72. Pippard A. 1990 The elastic arch and its modes of instability. *Eur. J. Phys.* **11**, 359. (doi:10.1088/0143-0807/11/6/008)
73. Patricio P, Adda-Bedia M, Amar MB. 1998 An elastica problem: instabilities of an elastic arch. *Physica D* **124**, 285–295. (doi:10.1016/S0167-2789(98)00203-6)
74. Das K, Batra RC. 2009 Pull-in and snap-through instabilities in transient deformations of microelectromechanical systems. *J. Micromech. Microeng.* **19**, 035008. (doi:10.1088/0960-1317/19/3/035008)
75. Pandey A, Moulton DE, Vella D, Holmes DP. 2014 Dynamics of snapping beams and jumping poppers. *Europhys. Lett.* **105**, 24001. (doi:10.1209/0295-5075/105/24001)
76. Sano TG, Wada H. 2018 Snap-buckling in asymmetrically constrained elastic strips. *Phys. Rev. E* **97**, 013002. (doi:10.1103/PhysRevE.97.013002)
77. Gomez M, Moulton DE, Vella D. 2017 Critical slowing down in purely elastic 'snap-through' instabilities. *Nat. Phys.* **13**, 142–145. (doi:10.1038/nphys3915)
78. Gomez M, Moulton DE, Vella D. 2019 Dynamics of viscoelastic snap-through. *J. Mech. Phys. Solids* **124**, 781–813. (doi:10.1016/j.jmps.2018.11.020)
79. O'Reilly OM. 2017 Kirchhoff's rod theory. In *Modeling nonlinear problems in the mechanics of strings and rods* (ed. OMO'Reilly), pp. 187–268. Cham, Switzerland: Springer.
80. Wang L, Kim Y, Guo CF, Zhao X. 2020 Hard-magnetic elastica. *J. Mech. Phys. Solids* **142**, 104045. (doi:10.1016/j.jmps.2020.104045)
81. Audoly B, Pomeau Y. 2010 *Elasticity and geometry: from hair curls to the non-linear response of shells*. Oxford, UK: Oxford University Press.
82. Abbasi A, Sano TM, Yan D, Reis PM. 2023 Snap buckling of bistable beams under combined mechanical and magnetic loading. Figshare. (doi:10.6084/m9.figshare.c.6373197)